



UvA-DARE (Digital Academic Repository)

Structured doping of upconversion nanosystems for biological applications

Wang, Y.

Publication date
2011

[Link to publication](#)

Citation for published version (APA):

Wang, Y. (2011). *Structured doping of upconversion nanosystems for biological applications*. [Thesis, fully internal, Universiteit van Amsterdam].

General rights

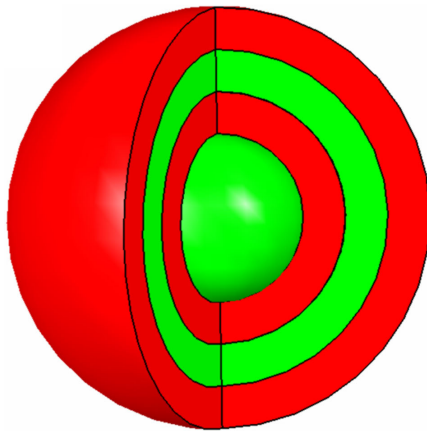
It is not permitted to download or to forward/distribute the text or part of it without the consent of the author(s) and/or copyright holder(s), other than for strictly personal, individual use, unless the work is under an open content license (like Creative Commons).

Disclaimer/Complaints regulations

If you believe that digital publication of certain material infringes any of your rights or (privacy) interests, please let the Library know, stating your reasons. In case of a legitimate complaint, the Library will make the material inaccessible and/or remove it from the website. Please Ask the Library: <https://uba.uva.nl/en/contact>, or a letter to: Library of the University of Amsterdam, Secretariat, P.O. Box 19185, 1000 GD Amsterdam, The Netherlands. You will be contacted as soon as possible.

CHAPTER 4

Structured Doping: A Strategy to Enhance Upconversion Luminescence for Bio-applications



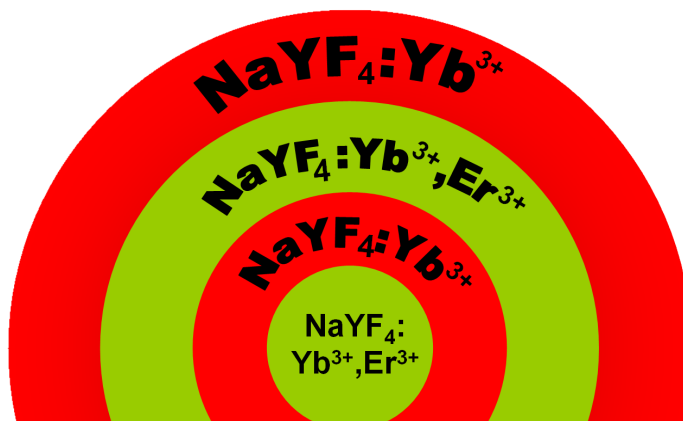
Chapter 4

Abstract: Luminescent upconversion nanoparticles doped with rare-earth ions have been intensively studied in recent years because of their unique properties, in particular their ability to perform infrared to visible photon conversion under CW illumination conditions. For *in vivo* applications their upconversion luminescence quantum yield is, however, not yet high enough, thereby impeding their potential medical applications. Rationally enhancing the emitter doping saturation threshold is a challenge to improve the upconversion luminescence. Here we report an approach to increase the number of the doped emitters in a nanoparticle that is based on the distribution of the emitters over several spatially separated areas. The spatial separation effectively blocks energy transfer between the separated areas. As far as the upconversion nanomaterial $\text{NaYF}_4:\text{Yb}^{3+},\text{Er}^{3+}$ is concerned we show that this approach enables us to more than double the so far accepted upper limit of the concentration quenching threshold of ~ 2 mol % for Er^{3+} , and raise it to 5 mol %, and thus enhance the upconversion luminescence significantly. Spectroscopic studies have been carried out to elucidate the upconversion mechanism, while studies of the efficiency with which singlet oxygen can be generated in conjugates of nanoparticles with photosensitizers demonstrate their suitability for medical applications. Our results suggest that our approach could very well be extended to other doped systems used for photonic applications.

Keywords: upconversion • nanoparticle • concentration quenching • singlet oxygen • lanthanides

4.1 Introduction

Rare earth ions doped luminescence upconversion nanoparticles (UCNPs) have attracted much attention in recent years owing to their superior spectroscopic properties, mainly arising from the existence of stable intermediate states. These properties can be used to ones advantage for applications in many fields, especially in biology and biomedicine.^[1] Amongst these materials, hexagonal-phase NaYF₄ is reported as one of the most efficient hosts for performing infrared-to-visible photon conversion in the doped rare-earth ions.^[2] However, the inherent requirement of low excitation density level in biological systems is a challenge for these photonic nanoparticles because of their low efficiency in the photon upconversion dynamics, which is not higher than several percent.^[3] Thus the optimization of every step in the excitation energy transfer route becomes vital. Hereto, one of the well-known approaches to enhance upconversion luminescence is to couple the nanoparticles to metallic surfaces or particles. In the vicinity of metal structures, the electric field distribution is altered, often referred to as local field effect. As a result, the excitation field as well as the emitted radiation can be enhanced. However, quenching by energy transfer and non-radiative relaxation in the metal is also possible.^[4] Another effective way to avoid emission quenching is to grow a homogeneous shell outside the UCNPs.^[5] The shell has essentially two functions: it protects the luminescent lanthanide ions in the core, especially those near the surface, from nonradiative energy transfer due to surface defects, which are more prevalent in nanoscale materials. In addition, the shell protects the ions from nonradiative relaxation processes involving the large vibrational energies of the solvent and surface-associated ligands. Core/shell nanoparticles offer clear advantages over similar uncoated materials in terms of protection of photoluminescence. Recently, active doping of both core and shell with ytterbium ions as sensitizer has led to further improvement in upconversion emission intensity.^[6] However, such core/shell architectures just protect the doped emitters from the influence of the surroundings such as quenching by surface defects, solvents, as well as the surface-bound ligands. It does not solve the problem of the low doping level. Concentration quenching is always observed at relatively low activator doping level. In the case of NaYF₄, it is usually accepted that the optimal dopant concentrations are approximately 20 mol% for sensitizer Yb³⁺ and 2 mol% for activator Er³⁺.^[7] Very recently it was reported that the intensity of upconversion emission could be increased by increasing the relative content of Yb³⁺ ions from 20 to 100%. However, as far as activators was concerned, a decrease in upconversion intensity was observed when the content is more than 2%.^[8]



Scheme 4.1. Depiction of nanoparticles with a sandwich-like architecture in which the doping activators are spatially separated. It contains four parts: the core ($\text{NaYF}_4:\text{Yb}^{3+}, \text{Er}^{3+}$), the first active shell ($\text{NaYF}_4:\text{Yb}^{3+}$), the second illuminate shell ($\text{NaYF}_4:\text{Yb}^{3+}, \text{Er}^{3+}$) and the final active shell ($\text{NaYF}_4:\text{Yb}^{3+}$).

Aiming at improving the doping level of the activators, and thus to enhance the upconversion luminescence, we establish a strategy of spatially separating the doping area. To this purpose a sandwich-like architecture (**Scheme 4.1**) has been developed of which the shell doped only with Yb^{3+} serves two purposes. On the one hand, it protects the luminescent ions against the influence of the surroundings and enables the transfer of the absorbed NIR photon energy to activators of both sides.^[6] On the other hand, it minimizes the energy transfer between the activators inside and outside. The latter aspect leads to the improvement of the concentration quenching threshold. It is demonstrated in the present work that such a structured doping strategy doubles the activator doping level as far as Er^{3+} is concerned. These findings open a new pathway to rationally improve the upconversion emission, and can facilitate the realization of potential biological applications of lanthanide ions doped nano-platforms, as well as enable new opportunities in energy harvesting and conversion.

4.2 Experiments

4.2.1 Chemicals

$(\text{CF}_3\text{COO})_3\text{Y}\cdot 3\text{H}_2\text{O}$, $(\text{CF}_3\text{COO})_3\text{Yb}\cdot 3\text{H}_2\text{O}$ and $(\text{CF}_3\text{COO})_3\text{Er}\cdot 3\text{H}_2\text{O}$ were purchased from *GFS chemicals*. CF_3COONa , oleylamine (OM), rose bengal (RB), 6-bromohexanoic acid, poly(allylamine) (PAAm), N-hydroxysuccinimide (NHS), 1-ethyl-3-(3-dimethylaminopropyl) carbodiimide (EDC) were purchased from *Aldrich*. 1,3-

diphenylisobenzofuran (DPBF) was purchased from *Fluka*. Ethanol and hexane were of analytical grade.

4.2.2 Nanoparticle synthesis

Nanoparticles of these three different models were all synthesized using a four-step method. The synthesis of NaYF₄:Yb³⁺,Er³⁺ bare core upconversion nanoparticles has been performed similar to the procedures reported previously (**Chapter 2**). Upon formation of the core nanoparticles, the other three shell precursors were mechanically injected into the reaction flask step by step, resulting in the final hexagonal-phase multi-shell nanoparticles.

4.2.3 Phase transfer of upconversion nanoparticles from hydrophobic to hydrophilic

The ligand exchange process was carried out to transfer hydrophobic UCNPs into hydrophilic ones using PAAm as ligand. 0.1 mL of PAAm solution (20 wt % in water) was dispersed in 10 mL ethanol. The hydrophobic UCNPs solution (~20 mg, purified and dispersed in 2 mL of cyclohexane) was mixed with the PAAm solution and stirred vigorously over 48 hours at 30 °C. After centrifugation, the obtained nanoparticles were redispersed in water. After phase transfer, the PAAm terminated UCNPs provide amino groups which can be used for covalently coupling carboxyl terminated molecules.

4.2.4 Conjugation of upconversion nanoparticles and rose bengal photosensitizer

First, the RB-NHS ester was synthesized as a previous protocol.^[9] Then, a 2.5 mg/mL solution of UCNPs was mixed with 1 mg RB-NHS ester at room temperature for 4 hours. UCNP-RB conjugates were dialyzed in water for two days to remove unreacted photosensitizer.

4.2.5 Singlet oxygen detection

¹O₂ was detected chemically using 1,3-diphenylisobenzofuran (DPBF) as a singlet oxygen sensor. Stock solutions of UCNP-RB conjugates were prepared by dispersing nanoconjugates in water. DPBF was prepared as a 8 mmol/L solution in water. All solutions were kept in the dark. In our experiments, 15 μL of the DPBF stock solution was added to a vial containing 2 mL of the photosensitizer stock solution and the mixture was mixed well. For detection, the mixture was irradiated at 980 nm using a CW diode laser.

4.2.6 Characterization

The structure and morphology of the UCNPs were characterized using a Bruker D8-advance X-ray diffractometer (XRD) with Cu Kα radiation ($\lambda = 1.5418 \text{ \AA}$), and a field emission scanning electron microscopy (FESEM, Hitachi, S-4800). Transmission electron microscopy (TEM) was performed on a Tecnai G2 F20 S-TWIN D573 electron microscope operated at 300 kV TEM. The upconversion emission spectra were acquired using a Jobin-Yvon LabRam Raman spectrometer system equipped with 1800 and 600 grooves/mm holographic gratings, respectively, and a Peltier air-cooled CCD detector.

Chapter 4

The samples were excited by a CW semiconductor diode laser at 980 nm. The upconversion luminescence spectra were measured under identical conditions in order to compare their relative emission intensities. The reduction in absorption was monitored as a function of time after irradiating samples with a 980 nm diode laser using a Hewlett-Packard/Agilent 8453 Diode-Array Biochemical Analysis UV-Vis Spectrophotometer. The luminescence kinetics was recorded with a 500 MHz Tektronix digital oscilloscope, using an optical parametric oscillator to provide excitation by a nanosecond pulse train at 480 nm.

4.3 Results and Discussion

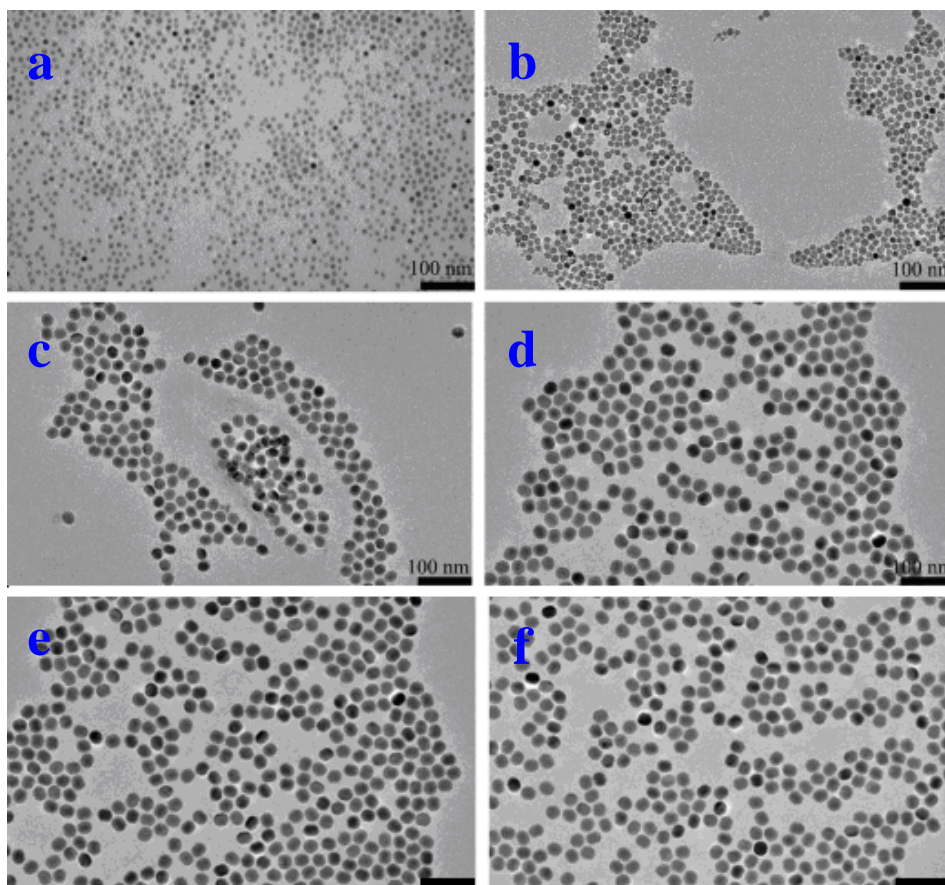


Figure 4.1. TEM images of the different structured nanoparticles: (a) core; (b) core/(active shell); (c) core/(active shell)/(luminescent shell); (d) core/(active shell)/(luminescent shell)/(active shell) (model A); (e) model B; (f) model C; scale bar = 100 nm.

The nanoparticles designed with a sandwich-like architecture (denoted as model **A**), were synthesized using the well-known thermolysis protocol, which proceeds via decomposition of metal trifluoroacetate precursors. The resulting hexagonal-phase nanoparticles had a mean particle size of 25 nm with a standard deviation of 0.6 nm. The core-only nanoparticles had a mean particle diameter of 10 nm (**Figure 4.1 (a)**) with an extremely narrow particle size distribution. The first active shell, second illuminating shell and the final active shell led to sizes of the nanoparticles of 15 nm, 20 nm, and 25 nm (see **Figure 4.1 (b), (c) and (d)**) with a narrow size distribution as shown in **Figure 4.2**. The X-ray diffraction (XRD) pattern for model **A** is shown in **Figure 4.3**. Obviously, the model **A** sample is pure hexagonal-phase NaYF₄ and well crystallized. During the course of the shell preparation, the synthesis was performed using a mechanical pump for the precise addition of the shell precursors to the reaction vessel to eliminate any variation caused by the rate of addition. Thus, the observed increase in size of the nanoparticles is attributed to the gradual growth of the shell around the core. From the difference in particle size of these four structures, every shell is estimated to be 4.6 nm thick.

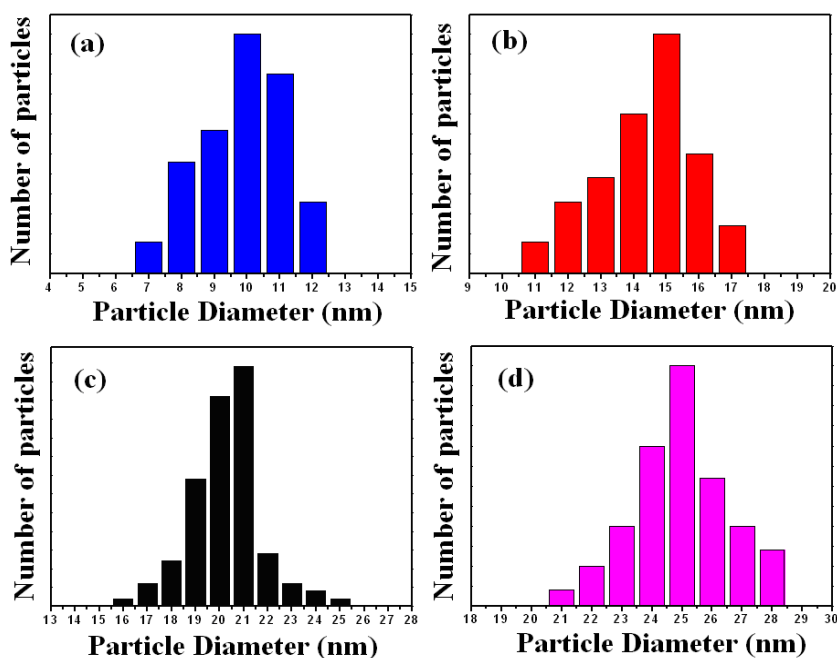


Figure 4.2. Histogram of the nanoparticle size distribution showing the different stages of nanoparticles (model **A**): **(a)** core; **(b)** core/(active shell); **(c)** core/(active shell)/(luminescent shell); **(d)** core/(active shell)/(luminescent shell)/(active shell).

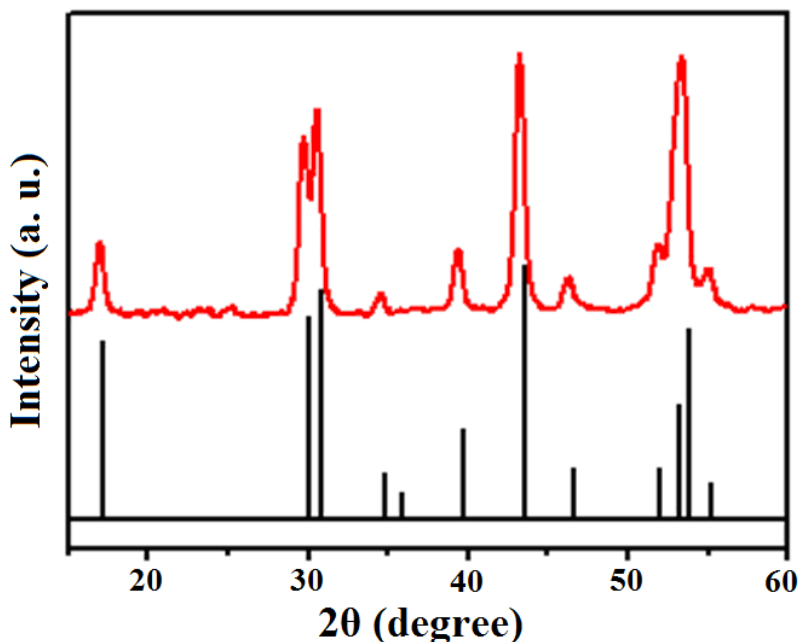
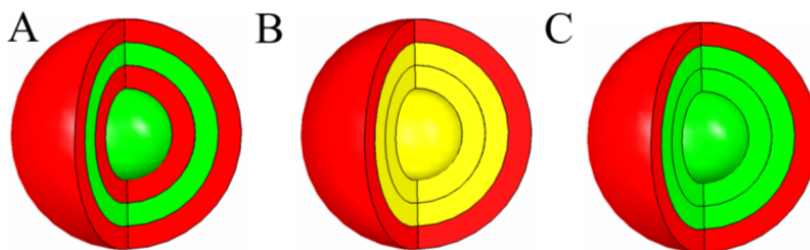


Figure 4.3. Experimental powder X-ray diffraction (XRD) pattern for the final products (model A) and the calculated line pattern for the hexagonal NaYF_4 phase.

To illustrate better the existence of the sandwich-type architecture and the advantage over the traditional core/shell structure, we have designed for comparison two different models **B** and **C** (see **Scheme 4.2**). Model **A** contains four parts: the core (NaYF_4 : 20% Yb^{3+} , 2% Er^{3+}), the first active shell (NaYF_4 : 20% Yb^{3+}), the second luminescent shell (NaYF_4 : 20% Yb^{3+} , 2% Er^{3+}) and the final active shell (NaYF_4 : 20% Yb^{3+}). Model **B** differs from model **A** by mixing the lanthanide trifluoroacetate precursors of the first three parts of model **A**, gradually growing the core (see **Scheme 4.2**, the yellow part in model **B**) until the same size of the first three parts in model **A** is reached, whereas the final active shell was kept unchanged. Compared with model **A**, model **B** has the same doped quantity but lower doping concentration. For model **C**, 2% Er^{3+} was doped into the first active shell, also forming a core (also see **Scheme 4.2**, the green part in model **C**) as big as the first three parts of model **A**, while the final active shell was kept the same. With this structure, model **C** has the same doping concentration but a higher number of emitters compared to model **A**. To guarantee that the nanoparticles of these three different models have the same size, the amount of the lanthanide trifluoroacetate precursors of every part and the synthetic approach were kept the same. TEM images of model **B** and **C** are shown in **Figure 4.1 (e) and (f)**.



Scheme 4.2. Structures of models *A*, *B* and *C*

Figure 4.4 shows the upconversion emission spectra of the three different UCNPs. In all cases, upconversion emission was observed in the green and red spectral regions following excitation at 980 nm. Green emission at 510 – 570 nm is well-known, and has been ascribed to transitions from the $^2H_{11/2}$ and $^4S_{3/2}$ excited states to the $^4I_{15/2}$ ground state (centred at 525 and 550 nm, respectively). Red emission between 630 – 680 nm is from the $^4F_{9/2}$ excited state to the ground state.^[10]

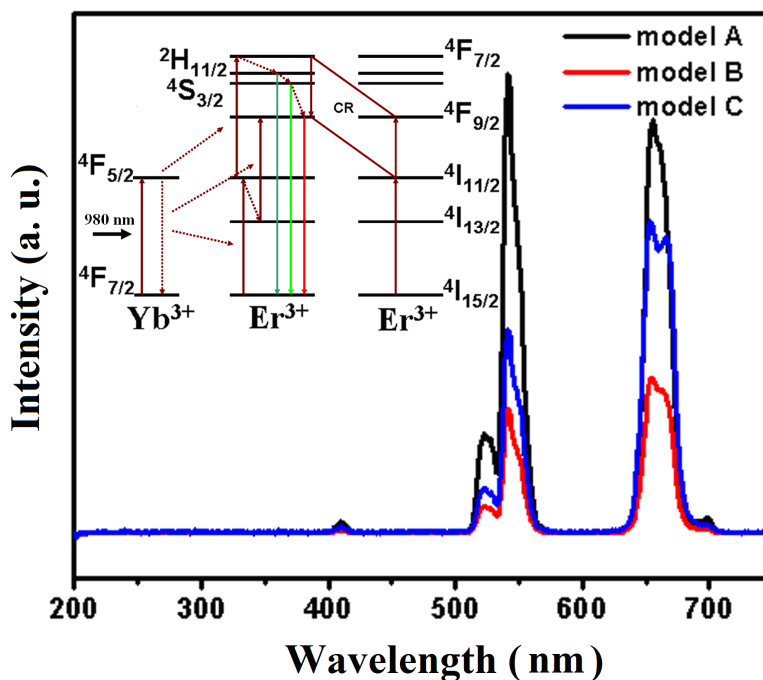


Figure 4.4. Upconversion luminescence spectra of colloidal nanoparticles with model *A* (black line), model *B* (red line) and model *C* (blue line). The inset shows the schematic illustration of the upconversion luminescence process with 980 nm excitation.

Chapter 4

The upconversion luminescence spectra also reveal distinct differences between these three models. The most obvious one is the emission intensity. The highest emission is observed in model **A** which is larger by a factor of approximately 3.5 in the green and 2.3 in the red compared to model **B**, and by a factor of 2.1 in the green and 1.1 in the red compared to model **C**. As we know, the distance between two neighbouring activators can significantly affect the photophysical properties of the nanoparticles, as is apparent from the upconversion luminescence spectra of models **B** and **C**. Both of them have a similar architecture with activators homogeneously distributed in the core, while the Er^{3+} concentration is larger in model **C** (2%) than in model **B** (less than 2%). We find that the intensity and the red to green (R/G) ratio observed for model **C** (R/G ratio = 2.15) is higher than observed for model **B** (R/G ratio = 1.70). For model **C**, the number of activators is higher than for model **A**, whereas the Er^{3+} concentration, and thus the distance between two neighbouring activators, is the same, however, the upconversion emission of model **C** is even weaker. Furthermore, the red to green (R/G) ratio in model **A** (R/G ratio = 1.15) is less than that in model **C** (R/G ratio = 2.15). It is interesting to note that compared to model **C**, model **A** has a much stronger upconversion luminescence and an even lower R/G ratio.

These spectral differences are related to the upconversion mechanism. The energy level ${}^4\text{F}_{9/2}$ for the red emission (${}^4\text{F}_{9/2} \rightarrow {}^4\text{I}_{15/2}$) can be populated via the following processes (see **Figure 4.4**):^[11] (i) direct population from the ${}^4\text{I}_{13/2}$ level, which can be populated through the nonradiative relaxation of the ${}^4\text{I}_{11/2}$ level, (ii) via nonradiative relaxation from the ${}^4\text{S}_{3/2}$ level, and (iii) by ${}^4\text{F}_{7/2} \rightarrow {}^4\text{F}_{9/2}$ and ${}^4\text{I}_{11/2} \rightarrow {}^4\text{F}_{9/2}$ cross-relaxation processes between two nearby Er^{3+} ions. The first two processes emphasize the importance of multiphonon relaxation, which is mainly caused by the presence of the organic groups on the surface of the nanoparticles. In this case, the particles of these three different models are all coated with an active shell and have the same size, thus we do not expect much difference in the red emission populated by multiphonon relaxation. The cross-relaxation, which is dependent on the distance between two neighbouring activators, is then the one that is responsible for the difference in red emission. From this point of view, the Er^{3+} - Er^{3+} distance in model **B** is less than that in model **C**. Therefore, the red to green (R/G) ratio of model **B** (R/G ratio = 1.70) is less than that of model **C** (R/G ratio = 2.15). As far as models **A** and **C** are concerned, they have the same Er^{3+} - Er^{3+} distance but a different architecture. The red to green (R/G) ratio of model **A** (R/G ratio = 1.15) is less than that of model **C** (R/G ratio = 2.15). It is reasonable to assume that in model **A** the sandwich-like architecture hampers the cross-relaxation process in the interface area, and thereby lifts the concentration quenching threshold. This would lead to an enhancement of the overall upconversion luminescence and a relatively low R/G ratio.

It is well known that a high doping level can lead to deleterious resonant energy transfer, increasing the possibility of the excitation energy being trapped by quench centers. The concentration of activator ions should thus be kept low and precisely adjusted

to avoid the quenching effect. Therefore, in Yb^{3+} , Er^{3+} co-doped NaYF_4 systems the sensitizer content is normally kept high (about 20%), while the activator content is relatively low (about 2%), minimizing excitation energy loss. This was indeed proved by further increasing the doping level of model C to 3%, where the concentration quenching happened (see **Figure 4.5**) in line with previous reports.^[8] In principle, the growth of the activator doping concentration would lead to an increase of the R/G ratio,^[12] which is also substantiated by comparing the R/G ratio of model B and C. However, for model A, the overall upconversion luminescence is the highest among the three model systems, whereas the R/G ratio is the lowest when the Er^{3+} concentration is 2%. This is a promising sign that architectures like model A may have the capacity of containing more activators.

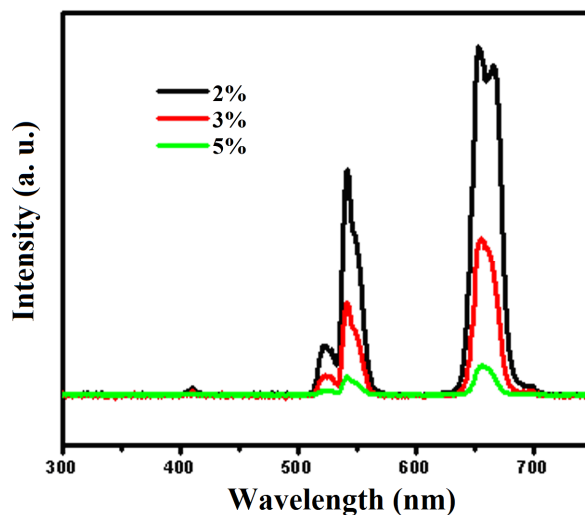


Figure 4.5. Upconversion luminescence spectra of colloidal NaYF_4 nanoparticles with structure of model C co-doped with 20% Yb^{3+} and various concentrations of Er^{3+} ions (2%, 3% and 5%) under diode laser excitation at 980 nm.

To validate this hypothesis, we gradually increased the doping quantity of the Er^{3+} ions. **Figure 4.6** shows the upconversion luminescence spectra of colloidal NaYF_4 nanoparticles co-doped with Yb^{3+} (20%) and various concentrations of Er^{3+} ions (2, 3, 5, 7, and 10%) when excited at 980 nm with a CW laser. As seen in **Figure 4.6**, the absolute intensities of the green and red emissions rise with doping concentration up to 5% and then decrease. At the same time, the red emission grows faster than the green one. The 2 mol % sample has a red/green intensity ratio of 1.15. As the doping concentration increases, the red component becomes more prominent. For example, for the 3 mol % and 5 mol % samples, the ratio becomes 2.25 and 3.05, respectively. When the concentration of Er^{3+} ions increases to more than 5%, the distance between Er^{3+} ions is so close that

Chapter 4

concentration quenching becomes important, causing the intensity to drop down by 7% and 10%, respectively. Thus it is evident that the structured doping approach can indeed lift the threshold of concentration quenching.

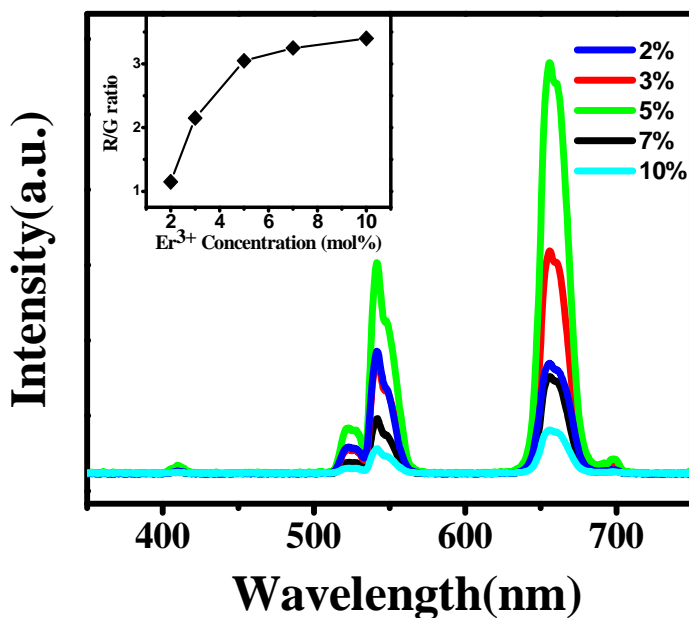


Figure 4.6. Upconversion luminescence spectra of colloidal NaYF_4 nanoparticles co-doped with 20% Yb^{3+} and various concentrations of Er^{3+} ions (2% to 10%) under diode laser excitation at 980 nm with R/G ratio shown in the inset.

To understand further the underlying mechanism, we have studied the temporal behaviour of the green emission (**Figure 4.7**). Under direct excitation of 488 nm, the transition ${}^2\text{H}_{11/2}$ (${}^4\text{S}_{3/2}$) \rightarrow ${}^4\text{I}_{15/2}$ (~ 540 nm), which reflects directly the de-population process of the emissive states, has been monitored in time. The decay curves can be adequately fitted with a bi-exponential function. In all the three models, the fast component τ_1 is around 10 μs , whereas the slow component τ_2 changes from 69.4 μs (model **A**), to 54.7 μs (model **B**) to 36.8 μs (model **C**). The fast component τ_1 , to which the outer layer Er^{3+} ions mainly contribute, varies little among **A**, **B**, and **C** because the distribution of the Er^{3+} ions in the outer layer is similar in all three models. On the other hand, the long component, τ_2 , reflects more the properties of activators in the inner shell and therefore is much more model-dependent.^[13]

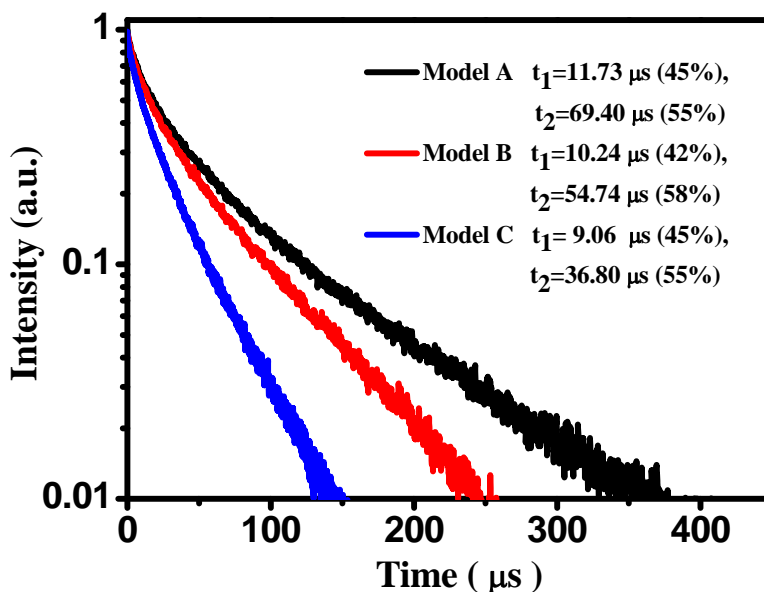


Figure 4.7. The decay curves of models A , B and C with 488 nm excitation.

A high doping level can lead to deleterious energy transfer, resulting in quenching of excitation energy. The Er^{3+} concentration in model **B** is less than that in model **C**. Therefore, the lifetime of model **B** is longer than that of model **C**. For the same Er^{3+} concentration but different doping structure, e.g. models **A** and **C**, the lifetime of **A** is longer than that of **C**. This indicates that the emitters in model **A** are separated by an active intermediate layer that only contains Yb^{3+} . The excitation energy of the luminescence centers of the inner layer can therefore not be effectively transferred to surface quench centers via resonant energy transfer between activator centers, thus extending the lifetime.

To show that this sandwich-like nanoparticle architecture is favourable for the application of the UCNPs in biology/biomedicine, we have developed UCNP-RB nanoconjugates to illustrate the increased efficiency of singlet oxygen generation. RB is one of the clinically used photosensitizers in cancer therapy. When the UCNP-RB nanoconjugates are irradiated by infrared light, the visible upconversion emission from the nanoparticles will be transferred to the photosensitizing molecules coated on their surfaces based on fluorescence resonance energy transfer (FRET). Subsequently, excited photosensitizing molecules will interact with surrounding ground-state oxygen molecules, generating the very aggressive $^1\text{O}_2$, which attacks the targeted cancer cells. Theoretically,

Chapter 4

the increase of upconversion emission should promote the singlet-oxygen generation. As a proof of concept, we carried out experiments to demonstrate the feasibility of this design.

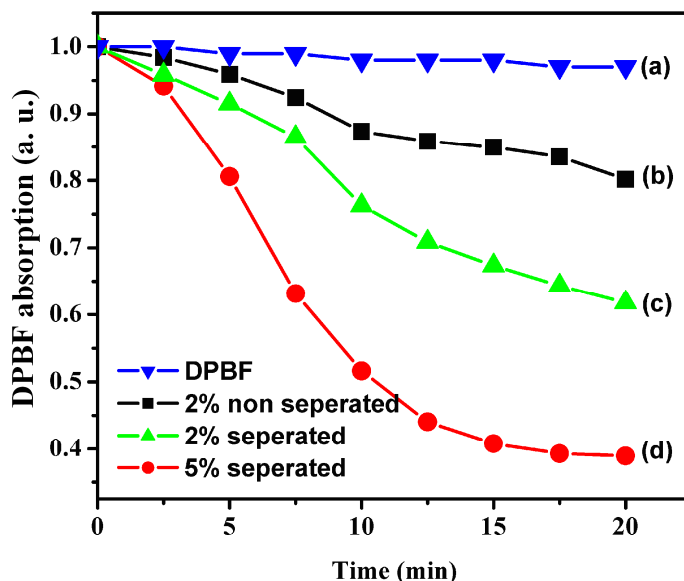


Figure 4.8. The decay curves of absorption of DPBF at 410 nm caused by (a) pure DPBF, (b) 2% non-separated UCNPs-RB conjugates, (c) 2% separated UCNPs-RB conjugates, and (d) 5% separated UCNPs-RB conjugates in ethanol as a function of irradiation time. The excitation wavelength is 980 nm.

Singlet-oxygen generation was confirmed by a chemical method using DPBF as a detector. DPBF reacts irreversibly with singlet oxygen, causing a decrease in the absorption at 410 nm.^[14] **Figure 4.8** shows the decrease in absorption intensity at 410 nm in different samples (pure DPBF, DPBF/2% non-separated UCNPs-RB, DPBF/2% separated UCNPs-RB, and DPBF/5% separated UCNPs-RB), as a function of exposure time under CW 980 nm laser irradiation. The slope of the curve is roughly proportional to the efficiency of generated singlet oxygen.^[15] It is therefore confirmed that the sandwich-like architecture can indeed greatly improve the biological behaviour of the rare earth ions doped nanoparticles.

4.4 Conclusions

In conclusion, we have put forward and validated a new strategy to improve the upconversion emission of rare earth ions doped nanoparticles by spatially separating the areas in which the activators are doped. It is demonstrated that such a design can improve

the upconversion luminescence by minimizing the energy transfer between the activators inside and outside, improving the threshold for concentration quenching. This strategy might pave a new pathway to rationally designing nanoparticles with high upconversion luminescence and promote relevant biological application.

4.5 Acknowledgments

This work was financially supported by NSFC of China (11004189, 10904142), the exchange program between CAS of China and KNAW of the Netherland.

4.6 References

-
- 1 (a) Combined Optical and MR Bioimaging Using Rare Earth Ion Doped NaYF₄ Nanocrystals. R. Kumar, M. Nky, T.Y. Ohulchansky, C.A. Flask, and P.N. Prasad; *Adv. Funct. Mater.*, **2009**, *19*, 853-859; (b) Upconversion Nanoparticles in Biological Labeling, Imaging, and Therapy. F. Wang, D. Banerjee, Y. Liu, X. Chen, and X. Liu; *Analyst*, **2010**, *135*, 1839-1854; (c) Luminescent Rare Earth Nanomaterials for Bioprobe Applications. J. Shen, L. Sun, and C. Yan; *Dalton Trans.*, **2008**, 5687-5697; (d) Versatile Photosensitizers for Photodynamic Therapy at Infrared Excitation. P. Zhang, W. Steelant, M. Kumar, and M. Scholfield; *J. Am. Chem. Soc.*, **2007**, *129*, 4526-4527; (e) Versatile Synthesis Strategy for Carboxylic Acid-functionalized Upconverting Nanophosphors as Biological Labels. Z. Chen, H. Chen, H. Hu, M. Yu, F. Li, Q. Zhang, Z. Zhou, T. Yi, and C. Huang; *J. Am. Chem. Soc.*, **2008**, *130*, 3023-3029; (f) High Contrast in Vitro and in Vivo Photoluminescence Bioimaging Using Near Infrared to Near Infrared Up-Conversion in Tm³⁺ and Yb³⁺ Doped Fluoride Nanophosphors. M. Nyk, R. Kumar, T.Y. Ohulchansky, E.J. Bergey, and P.N. Prasad; *Nano Lett.*, **2008**, *8*, 3834-3838; (g) Remote-Control Photorelease of Caged Compounds Using Near-Infrared Light and Upconverting Nanoparticles. C.J. Carling, F. Nourmohammadian, J.C. Boyer, and N.R. Branda; *Angew. Chem. Int. Ed.*, **2010**, *49*, 3782-3785; (h) Fluorescence Resonant Energy Transfer Biosensor Based on Upconversion-Luminescent Nanoparticles. L. Wang, R. Yan, Z. Huo, L. Wang, J. Zeng, J. Bao, X. Wang, Q. Peng, and Y. Li; *Angew. Chem. Int. Ed.*, **2005**, *44*, 6054-6057; (i) Optical Ammonia Sensor Based on Upconverting Luminescent Nanoparticles. H.S. Mader, O. S. Wolfbeis; *Anal. Chem.*, **2010**, *82*, 5002-5004; (j) Rare Earth Fluoride Nano-/Microcrystals: Synthesis, Surface Modification and Application. C.X. Li, J. Lin; *J. Mater. Chem.*, **2010**, *20*, 6831-6847; (k) Design of a Highly Sensitive and Specific Nucleotide Sensor Based on Photon Upconverting Particles. P. Zhang, S. Rogelj, K. Nguyen, and D. Wheeler; *J. Am. Chem. Soc.*, **2006**, *128*, 12410-12411; (l) Temperature Sensing Using Fluorescent Nanothermometers. F. Vetrone, R. Naccache, A. Zamarrón, A.J. de la Fuente, F. Sanz-Rodríguez, L.M.

- Maestro, E.M. Rodriguez. D. Jaque, J.G. Solé, and J.A. Capobianco; *ACS Nano*, **2010**, *4*, 3254-3258; (m) Upconverting Nanoparticles as Nanotransducers for Photodynamic Therapy in Cancer Cells. D.K. Chatterjee, Y. Zhang; *Nanomedicine*, **2008**, *3*, 73-82; (n) Biocompatibility of Silica Coated NaYF₄ Upconversion Fluorescent Nanocrystals. R.A. Jalil, Y. Zhang; *Biomaterials*, **2008**, *29*, 4122-4128; (o) “Intelligent” Fingerprinting: Simultaneous Identification of Drug Metabolites and Individuals by Using Antibody-Functionalized Nanoparticles. R. Leggett, E.E. Lee-Smith, S.M. Jickells, and D.A. Russell; *Angew. Chem. Int. Ed.*, **2007**, *46*, 4100; (p) Upconverting Luminescent Nanoparticles for Use in Bioconjugation and Bioimaging. H.S. Mader, P. Kele, S.M. Saleh, and O.S. Wolfbeis; *Current Opinion in Chemical Biology*, **2010**, *14*, 582-596
- 2 (a) Synthesis of Oil-Dispersible Hexagonal-Phase and Hexagonal-Shaped NaYF₄:Yb, Er Nanoplates. Y. Wei, F.Q. Lu, X.R. Zhang, and D.P. Chen; *Chem. Mater.*, **2006**, *18*, 5733-5737; (b) Synthesis of Hexagonal-Phase NaYF₄:Yb,Er and NaYF₄:Yb,Tm Nanocrystals with Efficient Up-Conversion Fluorescence. G.S. Yi, G.M. Chow; *Adv. Funct. Mater.*, **2006**, *16*, 2324-2329; (c) High-Quality Sodium Rare-Earth Fluoride Nanocrystals: Controlled Synthesis and Optical Properties. H.X. Mai, Y.W. Zhang, R. Si, Z.G. Yan, L.D. Sun, L.P. You, and C.H. Yan; *J. Am. Chem. Soc.*, **2006**, *128*, 6426-6436; (d) Synthesis of Polyethylenimine/NaYF₄ Nanoparticles with Upconversion Fluorescence. F. Wang, D.K. Chatterjee, Z.Q. Li, and Y. Zhang; *Nanotechnology*, **2006**, *17*, 5786; (e) Synthesis and Upconversion Luminescence of Hexagonal-Phase NaYF₄:Yb, Er³⁺ Phosphors of Controlled Size and Morphology. J. H. Zeng, J. Su, Z.H. Li, R.X. Yan, and Y.D. Li; *Adv. Mater.*, **2005**, *17*, 2119-2123; (f) Synthesis of Colloidal Upconverting NaYF₄ Nanocrystals Doped with Er³⁺, Yb³⁺ and Tm³⁺, Yb³⁺ via Thermal Decomposition of Lanthanide Trifluoroacetate Precursors. J.C. Boyer, F. Vetrone, L.A. Cuccia, and J.A. Capobianco; *J. Am. Chem. Soc.*, **2006**, *128*, 7444-7445; (g) A Strategy to Protect and Sensitize Near-Infrared Luminescent Nd³⁺ and Yb³⁺: Organic Tropolonate Ligands for the Sensitization of Ln³⁺-Doped NaYF₄ Nanocrystals. J. Zhang, C. M. Shade, D. A. Chengelis, and S. Petoud; *J. Am. Chem. Soc.*, **2007**, *129*, 14834-14835; (h) Lanthanide-Doped NaYF₄ Nanocrystals in Aqueous Solution Displaying Strong Up-Conversion Emission. H. Schäfer, P. Ptacek, K. Kompe, and M. Haase; *Chem. Mater.*, **2007**, *19*, 1396-1400; (i) Highly Uniform and Monodisperse β-NaYF₄:Ln³⁺ (Ln = Eu, Tb, Yb/Er, and Yb/Tm) Hexagonal Microprism Crystals: Hydrothermal Synthesis and Luminescent Properties. C. Li, Z. Quan, J. Yang, P. Yang, and J. Lin; *Inorg. Chem.*, **2007**, *46*, 6329-6337; (j) Ionothermal Synthesis of Hexagonal-phase NaYF₄: Yb³⁺,Er³⁺/Tm³⁺ Upconversion Nanophosphors. X.M. Liu, J.W. Zhao, Y.J., Sun, K. Song, X.G. Kong, and H. Zhang; *Chem. Commun.*, **2009**, 6628.

-
- 3 (a) Absolute Quantum Yield Measurements of Colloidal NaYF₄: Er³⁺, Yb³⁺ Upconverting Nanoparticles. J.C. Boyer, F.C.J.M. Van Veggel; *Nanoscale*, **2010**, 2, 1417-1419; (b) Quantum Dot–Fluorescent Protein Pairs as Novel Fluorescence Resonance Energy Transfer Probes. A.M. Dennis, G. Bao; *Nano Lett.*, **2008**, 8, 1439-1445.
- 4 (a) Plasmon-Enhanced Upconversion in Single NaYF₄:Yb³⁺/Er³⁺ Codoped Nanocrystals. S. Schietinger, T. Aichele, H.Q. Wang, T. Nann, and O. Benson; *Nano Lett.*, **2010**, 10, 134-138; (b) Plasmonic Modulation of the Upconversion Fluorescence in NaYF₄:Yb/Tm Hexaplate Nanocrystals Using Gold Nanoparticles or Nanoshells. H. Zhang, Y.J. Li, I.A. Ivanov, Y.Q. Qu, Y. Huang, and X.F. Duan; *Angew Chem. Int. Ed.*, **2010**, 49, 2865-2868.
- 5 (a) Highly Efficient Multicolor Up-Conversion Emissions and Their Mechanisms of Monodisperse NaYF₄:Yb,Er Core and Core/Shell-Structured Nanocrystals. H.X. Mai, Y.W. Zhang, L.D. Sun, and C.H. Yan; *J. Phys. Chem. C*, **2007**, 111, 13721-13729; (b) Water-Soluble NaYF₄:Yb,Er(Tm)/NaYF₄/Polymer Core/Shell/Shell Nanoparticles with Significant Enhancement of Upconversion Fluorescence. G.S. Yi and G.M. Chow; *Chem. Mater.*, **2007**, 19, 341-343; (c) Synthesis, Characterization, and Spectroscopy of NaGdF₄: Ce³⁺, Tb³⁺/NaYF₄ Core/Shell Nanoparticles. J.C. Boyer, J. Gagnon, L.A. Cuccia, and J.A. Capobianco; *Chem. Mater.*, **2007**, 19, 3358-3360; (d) Synthesis and Optical Properties of KYF₄/Yb, Er Nanocrystals, and their Surface Modification with Undoped KYF₄. H. Schafer, P. Ptacek, O. Zerzouf, and M. Haase; *Adv. Funct. Mater.*, **2008**, 18, 2913-2918; (e) Synthesis of Hexagonal-Phase Core–Shell NaYF₄ Nanocrystals with Tunable Upconversion Fluorescence. H.S. Qian and Y. Zhang; *Langmuir*, **2008**, 24, 12123-12125; (f) Upconversion Luminescence of β-NaYF₄: Yb³⁺, Er³⁺@β-NaYF₄ Core/Shell Nanoparticles: Excitation Power Density and Surface Dependence. Y. Wang, L.P. Tu, J.W. Zhao, Y.J. Sun, X.G. Kong, and H. Zhang; *J. Phys. Chem. C*, **2009**, 113, 7164-7169; (g) Direct Evidence of a Surface Quenching Effect on Size-Dependent Luminescence of Upconversion Nanoparticles. F. Wang, J. Wang, and X. G. Liu; *Angew Chem. Int. Ed.*, **2010**, 49, 7456-7460.
- 6 The Active-Core/Active-Shell Approach: A Strategy to Enhance the Upconversion Luminescence in Lanthanide-Doped Nanoparticles. F. Vetrone, R. Naccache, V. Mahalingam, C.G. Morgan, and J.A. Capobianco; *Adv. Funct. Mater.*, **2009**, 19, 2924-2929.
- 7 (a) Simultaneous Phase and Size Control of Upconversion Nanocrystals through Lanthanide Doping. F. Wang, Y. Han, C.S. Lim, Y.H. Lu, J. Wang, M.H. Hong, and X.G. Liu; *Nature*, **2010**, 463, 1061; (b) Hexagonal Sodium Yttrium Fluoride Based Green and Blue Emitting Upconversion Phosphors. K.W. Kramer, D. Biner, G. Frei, H.U. Gudel, M.P. Hehlen, and S.R. Luthi; *Chem. Mater.*, **2004**, 16, 1244-1251.

Chapter 4

- 8 Ultrasmall Monodisperse NaYF₄:Yb³⁺/Tm³⁺ Nanocrystals with Enhanced Near-Infrared to Near-Infrared Upconversion Photoluminescence. G.Y. Chen, T.Y. Ohulchanskyy, R. Kumar, H. Agren, and P.N. Prasad; *ACS Nano*, **2010**, *4*, 3163-3168.
- 9 Light-induced proteolysis of myosin heavy chain by Rose Bengal-conjugated antibody complexes. K.A. Conlon, M. Berrios; *Journal of Photochemistry and Photobiology B: Biology*, **2001**, *65*, 22-28.
- 10 Recent Advances in the Chemistry of Lanthanide-Doped Upconversion Nanocrystals. F. Wang, X.G. Liu; *Chem. Soc. Rev.*, **2009**, *38*, 976-989.
- 11 Upconversion and Anti-Stokes Processes with f and d Ions in Solids. F. Auzel; *Chem. Rev.*, **2004**, *104*, 139-174.
- 12 Controlled Synthesis, Formation Mechanism, and Great Enhancement of Red Upconversion Luminescence of NaYF₄: Yb³⁺,Er³⁺ Nanocrystals/Submicroplates at Low Doping Level. J.W. Zhao, Y.J. Sun, X.G. Kong, and H. Zhang; *J. Phys. Chem. B*, **2008**, *112*, 15666.
- 13 Morphology-Dependent Upconversion Luminescence of ZnO:Er³⁺ Nanocrystals. Y.J. Sun, Y. Chen, L.J. Tian, Y. Yu, X.G. Kong, Q.H. Zeng, Y.L. Zhang, and H. Zhang; *Journal of Luminescence*, **2008**, *128*, 15-21.
- 14 (a) Singlet Oxygen Quantum Yields of Different Photosensitizers in Polar Solvents and Micellar Solutions. W. Spiller, H. Kliesch, D. Wohrele, S. Hackbarth, B. Roder, and G.J. Schnurpfeil; *J. Porphyrins Phthalocyanines*, **1998**, *2*, 145; (b) Methylene Blue-Containing Silica-Coated Magnetic Particles: A Potential Magnetic Carrier for Photodynamic Therapy. D.B. Tada, L.L.R. Vono, E.L. Duarte, R. Itri, P.K. Kiyohara, M.S. Baptista, and L.M. Rossi; *Langmuir*, **2007**, *23*, 8194-8199.
- 15 (a) Nanomaterials and Singlet Oxygen Photosensitizers: Potential Applications in Photodynamic Therapy. S. Wang, R. Gao, F. Zhou, and M. Selke; *J. Mater. Chem.*, **2004**, *14*, 487-493; (b) Organically Modified Silica Nanoparticles with Covalently Incorporated Photosensitizer for Photodynamic Therapy of Cancer. T.Y. Ohulchanskyy, I. Roy, L.N. Goswami, Y. Chen, E.J. Bergey, R.K. Pandey, A.R. Oseroff, and P.N. Prasad; *Nano. Lett.*, **2007**, *7*, 2835-2842; (c) Ceramic-Based Nanoparticles Entrapping Water-Insoluble Photosensitizing Anticancer Drugs: A Novel Drug-Carrier System for Photodynamic Therapy. I. Roy, T.Y. Ohulchanskyy, H.E. Pudavar, E.J. Bergey, A.R. Oseroff, J. Morgan, T.J. Dougherty, and P.N. Prasad; *J. Am. Chem. Soc.*, **2003**, *125*, 7860-7865.